

# All-optical autoencoder machine learning framework using diffractive processors

Peijie Feng<sup>1</sup>, Yong Tan<sup>2,3</sup>, Mingzhe Chong<sup>1</sup>, Lintao Li<sup>2</sup>, Zongkun Zhang<sup>1</sup>, Fubei Liu<sup>2</sup>, Yunhua Tan<sup>1</sup> and Yongzheng Wen<sup>2,3</sup>

<sup>1</sup>School of Electronics, Peking University, Beijing, 10087, China

<sup>2</sup>School of Materials Science and Engineering, Tsinghua University, Beijing, 10084, China

<sup>3</sup>Wuzhen Lab, Jia Xing, 314501, China

Correspondence: Yunhua Tan Email: [tanggeric@pku.edu.cn](mailto:tanggeric@pku.edu.cn) & Yongzheng Wen Email: [wenyzheng@tsinghua.edu.cn](mailto:wenyzheng@tsinghua.edu.cn)

## Abstract

Diffractive deep neural network (D<sup>2</sup>NN), known for its high speed, low power consumption, and strong parallelism, has been widely applied across various fields, including pattern recognition, image processing, and image transmission. However, existing network architectures primarily focus on data representation within the original domain, with limited exploration of the latent space, thereby restricting the information mining capabilities and multifunctional integration of D<sup>2</sup>NNs. Here, we propose an all-optical autoencoder (OAE) framework that can encode the input wavefield into a prior shape distribution in the latent space and decode the encoded pattern back to the original wavefield. By leveraging the non-reciprocal property of D<sup>2</sup>NN, the OAE models function as encoders in one direction of wave propagation and as decoders in the opposite direction. We further apply the models to three key areas: image denoising, noise-resistant reconfigurable image classification, and image generation. Proof-of-concept experiments have been conducted to validate numerical simulations. Our OAE framework fully exploits the potential of latent space representations, enabling a single set of diffractive processors to simultaneously achieve image reconstruction, representation, and generation. It can be viewed as both a counterpart and an extension of the electronic autoencoder model. This work not only offers fresh insights into the design of optical generative models but also paves the way for developing and applying multifunctional, highly integrated, and general optical intelligent systems.

## Introduction

Deep learning, a subset of machine learning, has achieved remarkable performance in various fields over the past decade, including digital image processing<sup>1,2</sup>, natural language processing<sup>3</sup>, pattern recognition<sup>4,5</sup>, intelligent device design<sup>6</sup>, and the discovery of physical laws<sup>7</sup>. By employing multilayered artificial neural networks with a large number of parameters to simulate complex brain processes, deep learning enables computers to automatically extract features and learn from extensive datasets. Among the techniques of deep learning, generative models have garnered significant attention recently due to the success of large language models (LLMs)<sup>8</sup>. Typical models such as autoencoders (AEs)<sup>9</sup>, generative adversarial networks (GANs)<sup>10</sup>, and transformers<sup>11</sup>, essentially adhere to the encoding-decoding framework. By designing appropriate model structures and loss functions, a set of encoders and decoders is trained to extract enhanced data representations in latent space from raw data, revealing its inherent characteristics. By further leveraging the latent representations, generative models have demonstrated significant application potential in the field of data generation, such as artistic content creation<sup>12</sup>, text generation<sup>13</sup>, and speech synthesis<sup>14</sup>.

However, with the explosive growth in model scale and data volume, the bottleneck of computational power and storage capacity imposed by Moore's Law, coupled with the vast power consumption associated with network operations, hinder further advancements in deep learning model performance<sup>15,16</sup>. To address these limitations, optical neural networks (ONNs), which utilize the unique properties of light to achieve high speed, ultra-wide bandwidth, and energy-efficient computations, is proposed as a promising alternative<sup>17-22</sup>. The deep diffractive neural network (D<sup>2</sup>NN) is a prominent example of ONNs, utilizing light diffraction to establish connections and diffractive layers to modulate information<sup>23</sup>. And hypersurfaces provide an ultra-thin optical platform to implement diffractive layers<sup>24,25</sup>. Composed of numerous diffractive neurons, they enable subwavelength resolution control of light phase and amplitude, supporting the development of miniaturized and integrated intelligent optical systems.

Recent advances in D<sup>2</sup>NN have demonstrated its potential for efficient execution of deep learning tasks in the photonic domain. Within the realm of pattern recognition, D<sup>2</sup>NNs have been applied to image classifications<sup>26-31</sup>, sorting orbital angular momentum (OAM) beams<sup>32</sup>, and estimating the directions of arrival (DOA) of waves<sup>33,34</sup>. These applications require D<sup>2</sup>NNs to accurately recognize different types of input wavefields and focus the output on corresponding locations to achieve optical recognition. In the field of light computation, D<sup>2</sup>NNs are utilized to perform linear matrix calculations<sup>35,36</sup>, digital logic operations<sup>37</sup>, and trigonometric functions<sup>38</sup>, where they are trained to fit specialized calculators. Diffractive image processors implemented by D<sup>2</sup>NNs, such as image denoisers<sup>39</sup>, unidirectional imagers<sup>40,41</sup>, and super-resolution imagers<sup>42,43</sup> have been widely studied to tackle the high loss and complexity of traditional electronic systems. Beyond the above, there are also researches exploring the multiplexing mechanisms<sup>26,44-49</sup> and superior network structures<sup>28,30,50</sup> to enhance the parallelism, reconfigurability and scale of model.

However, these works focus solely on end-to-end representation of data in the original domain. Specifically, the input optical field carrying the original information passes through the D<sup>2</sup>NN and directly forms an artificially designed target wavefield at the output plane to perform a specific task. The latent data space, where data can be represented more concisely, is severely neglected. Although several studies have proposed optoelectronic encoder-decoder models that can transform the original information into latent space<sup>51,52</sup>, the cascading of electronic and optical modules imposes significant burdens due to optical-to-electrical conversion and mismatches. Recently, an all-optical VAE model implemented by spatial light modulator (SLM) is reported to optimize traditional fiber optic communication system<sup>53</sup>. The well-trained optical encoder and decoder are utilized to replace the optoelectronic hybrid transmitter and receiver, respectively. However, limited by the scenario, only the compression capability and reconstruction operation of the latent space is realized. All in all, current D<sup>2</sup>NNs have not fully explored the potential for

representation and application of the latent data space, which makes models tailored for specific tasks, lacking integration and versatility. Moreover, none of the existing works have truly achieved data generation in the optical domain.

In this article, we propose an all-optical autoencoder (OAE) machine learning framework, which consists of optical encoder and decoder that share a set of diffractive layers, achieving weight sharing. Benefiting from the non-reciprocal properties of the D<sup>2</sup>NN (See **Supplementary Materials**), Our framework acts as an encoder that transforms original image into encoded patterns in latent space along  $FOV_I \rightarrow FOV_{II}$  direction, while as a decoder that reconstructs the input from latent space along  $FOV_{II} \rightarrow FOV_I$  direction (See **Fig. 1(a)**). The encoded patterns are regularized by different prior shape distributions, giving rise to various modes of OAE framework (See **Fig. 1(b)**). The single optical autoencoder (SOAE) model and the multiple optical autoencoder (MOAE) model are basic modes. And the former encodes inputs from distinct classes into the same region, while the latter encodes them into separate, class-specific regions. Extended modes further design other six shapes of encoded region in the latent space. Additionally, we applied the SOAE model and MOAE model in three domains (See **Fig. 1(c)**). To achieve image denoising, we transmitted noisy images bidirectionally along  $FOV_I \rightarrow FOV_{II}$  and  $FOV_{II} \rightarrow FOV_I$ , utilizing the encoder and the decoder in a cascaded manner. This approach allows each diffractive layer to modulate the incident information twice, enhancing compactness of diffractive denoiser. We also constructed reconfigurable classifiers that can adapt to different datasets by altering pluggable classification layers behind the fixed encoder. Owing to the concise features extracted by the encoder, The classifiers demonstrate improved noise resistance performance. Finally, image generation, including hologram generation and conditional hologram generation, was achieved using the decoders of the SOAE and MOAE models, respectively. Conditional hologram generation here means that the category of the generated image is controlled by the spatial position of the encoded region, while the details of the image are determined by the encoded pattern. To the best of our knowledge, this is the first study that achieves conditional hologram generation in the optical domain, which remarkably improves the channel capacity and flexibility of hypersurface holography.

To validate the proposed OAE framework and its applications, we manufactured several sets of diffractive layers using 3D printing technology and conducted proof-of-concept experiments in the terahertz (THz) band. The experiments successfully proved the effectiveness of numerical simulations. Although our experiments were designed in the THz band, this framework can be universally extended to lower millimeter-wave bands or higher optical bands. For one thing, our framework employs the bidirectional multiplexing mechanism, using only a set of weights for self-encoding and decoding, broadens the scope of term auto. For another, the prior shape distribution of the latent space provides a new optical coding dimension for encoding design. Therefore, the OAE framework can be regarded as both a twin and an evolution of the electrical autoencoder model. Three application scenarios also demonstrate that the framework can simultaneously achieve data reconstruction, representation, and generation, embodying compactness and multifunctional integration. Our work will facilitate the design of optical generation models and versatile optical intelligent systems, which can be further applied to more typical tasks, such as image encryption, obstacle-avoiding optical communication, and off-axis holography.

## Results

In this article, we consistently define the forward direction as the light path from field of view I ( $FOV_I$ ) to  $FOV_{II}$ , while the backward direction is identified as reverse path ( $FOV_{II} \rightarrow FOV_I$ ).  $FOV_I$ , also called the original space, is shared by the original field and the reconstructed field. The encoding region in  $FOV_{II}$ , determined by the prior shape distribution, is referred to as the latent space. Our OAE framework functions as an encoder in the forward direction and as a decoder in the backward direction (See **Fig. 1(a)**), achieving self-encoding and decoding through a bidirectional multiplexing mechanism. Without loss of generality, the information in original space and latent space discussed in this section are represented using the amplitudes of complex fields. Specifically, the input images and reconstructed images in the original space, along with the encoded patterns in the latent space, are represented by the amplitudes of wavefields in their respective regions. Furthermore, our model can also convey information in the original space using the intensity or phase of light (See **Supplementary Fig. S16**) and represent encoded patterns using complex fields (See **Supplementary Fig. S5**). MNIST, EMNIST and Fashion datasets were utilized for model training and inference throughout this paper (See **Methods and Materials**).

### Performance of the MOAE model and the SOAE model

Two basic modes of the OAE framework, SOAE model and MOAE model, are firstly illustrated here. The encoded patterns of these two models are both a circle with a radius of 5, whose dimension is significantly smaller than that of original images (64 \* 64), resulting in a compression ratio of approximately 52. The SOAE model employs only a single encoding region for different categories of images, while the MOAE model assigns distinct encoding regions to different classes of images, mapping each class to its corresponding region. (See **Fig. 1(b)**). During model training, the original images were first passed through the model in the forward direction. Subsequently, the amplitude of the wavefield in the latent space was extracted as the encoding pattern. Finally, this encoding pattern was processed in the reverse direction through

the model to obtain the reconstructed images. To assist the model in achieving effective encoding and decoding reconstruction while ensuring system efficiency, appropriate loss functions are designed (See **Methods and Materials**). We also employed four metrics: MSE, SSIM, PSNR, and  $\eta$  (See **Methods and Materials**) to comprehensively evaluate the trained models. Among them, MSE, SSIM, and PSNR assess the quality of the reconstructed images, whereas  $\eta$  evaluates the forward and backward energy transmission efficiency of the models.

**Fig. 2 (a)** shows the phase profiles of the SOAE and MOAE models trained on the MNIST dataset. The SOAE model consists of five equally spaced phase-only modulation diffractive layers (N=5), with phase distributions that exhibit distinct center-focus characteristics, directing the original images toward the central encoding region. In contrast, the MOAE model includes six diffractive layers (N=6), with its phase distributions gradually transitioning from a single center to multiple centers, guiding the input images to converge on ten encoding regions (See **Methods and Materials** for detailed sizes of two models). The encoding (2nd and 4th rows) and decoding (3rd and 5th rows) results of these two models are presented in **Fig. 2 (b)**. The SOAE model compresses the image into the encoding region during forward encoding, while enlarges the compressed images to the original size during reverse decoding, which is similar to a convex lens. This lens-like characteristic grants the SOAE model strong generalization capabilities (See **Supplementary Fig. S2**). Therefore, our framework utilizes several planar diffraction layers designed by a data-driven deep learning algorithm to create a specialized convex lens, indicating that D<sup>2</sup>NN has the potential to extract general physical principles from specific datasets. The MOAE model transforms the original images into ten encoded patterns in the latent space. By reversely passing patterns in proper position through the model, it can also produce well-reconstructed images. The encoded patterns of this model possess encryption characteristics. (This figure only displays the encoded patterns in proper positions, and other patterns are illustrated in **Supplementary Fig. S3**.) **Fig. 2 (c)** shows the performance of both models trained on the EMNIST and Fashion datasets. Notably, the SOAE model trained on the Fashion dataset does not exhibit the lens-like characteristics. It is because the high complexity of the dataset makes it difficult for linear D<sup>2</sup>NN to extract general physical principles.

**Fig. 2 (d) and 2 (e)** show the convergence curves for training loss and three metrics of the SOAE and MOAE models, respectively. After several hundred of training epochs, two models both achieved stable convergence in training losses. However, the metrics indicate that the MOAE model exhibited greater fluctuations during training compared to the SOAE model, suggesting that the design of multiple encoding regions increased the difficulty of model optimization. Bar charts of metrics for both models trained on MNIST, EMNIST and Fashion datasets are illustrated in **Fig. 2 (f)**. The SOAE models trained on the MNIST and EMNIST datasets, which exhibit lens-like characteristics, demonstrated high image reconstruction quality and transmission efficiency (SSIM > 0.85, PSNR > 20 dB, and  $\eta$  > 50%). In contrast, due to the complexity of the Fashion dataset, the SOAE model trained on it showed the worst image reconstruction quality, with an MSE of 8.25e-5, SSIM of 0.73, and PSNR of 16.27dB. Furthermore,  $\eta_F$  of this model was also lower than that of previous two models, at only 10.90%. The performance of MOAE models across the three datasets was relatively similar (SSIM ~ 0.65, PSNR ~ 14.5 dB,  $\eta_F$  ~ 4%, and  $\eta_B$  ~ 20%). However, when compared to the SOAE models, the overall performance is degraded due to the more complex encoding task of achieving spatial multiplexing for ten encoding regions.

## Performance of the six extended modes

To further explore the representation capabilities of the latent space, we investigated other six different encoded patterns (see **Fig. 1 (b)**). All six models consist of five layers of phase only diffraction-only diffractive layers (N=5, See **Methods and Materials** for detailed sizes of extended models). **Fig. 3 (a)-(f)** illustrate the encoding (second row) and decoding (third row) performances of these models on the MNIST dataset. Closer model moves the  $FOV_{II}$  plane closer to the last diffraction layer ( $L_5$ ), reducing the original spacing from 34.8 mm (80 $\lambda$ ) to 11.6 mm (26.67 $\lambda$ ). By decreasing the layer distance, the model breaks the previous convex lens imaging rule, achieving encrypted encoding. Off-axis model shifts the circular encoding region leftward, enabling off-axis lens miniaturization imaging. Dually, by specifying the position of the reconstructed image on the  $FOV_I$  plane, off-axis reconstruction imaging can also be achieved (See **Supplementary Fig. S16**). Ring model sets the encoding region as an annulus with a width of 10, dispersing the originally centralized image information to the edges of the plane. Line model compresses the two-dimensional image into a one-dimensional encoded pattern with a length of 64, achieving spatial dimensionality reduction. V-fractal and S-fractal models designate the encoding regions as Vicsek and Sierpinski carpet fractal patterns<sup>54</sup>, respectively, with both set to order 3. These six extended patterns demonstrate that the OAE framework can flexibly manipulate the shapes of encoding regions and control the distribution of information in latent space. This feature can be further applied to fields such as obstacle-avoiding optical communication and image encryption.

Phase profiles of the six models are shown in **Fig. 3 (g)-(l)**. The propagation trend of light can be reflected by the phase profiles, particularly evident in the profile of last diffractive layer. Specifically, Closer model exhibits a central focusing characteristic, as its encoding pattern is located at the center of the region. Off-axis model demonstrates an off-center focusing characteristic due to its offset focusing pattern. Ring and Line models present annular and linear distributions that align with their respective encoding patterns. V-fractal and S-fractal models follow square arrangements corresponding to their respective fractal patterns. Bar charts of the metrics for these six models are displayed in **Fig. 3 (m)**. Line

model has the lowest image reconstruction quality and forward transmission efficiency, with an MSE of 3.40e-4, SSIM of 0.72, PSNR of 16.66 dB, and  $\eta_F$  of 34.72%, which is because the highest compression ratio of 64 in this mode makes feature extraction the most challenging. In contrast, Off-axis model achieves the highest image quality and system efficiency due to its off-axis convex lens imaging effect, with an MSE of 1.28e-4, SSIM of 0.88, PSNR of 20.45 dB,  $\eta_F$  of 61.05%, and  $\eta_B$  of 41.24%. By comparing with the results of the previous SOAE model, it can be concluded that when the convex lens-like features are extracted by OAE models, the model performance will excel in all aspects. The performance of the other four models is comparable, with an MSE of approximately 2e-4, SSIM around 0.75, PSNR around 19 dB,  $\eta_F$  around 45%, and  $\eta_B$  around 12%.

## Application 1: Image denoising

The SOAE model and MOAE model were further employed to three tasks to demonstrate the multifunctional integration characteristics of our framework. In this part, the encoders and decoders of the well-trained SOAE model and MOAE model were cascaded to serve as diffractive image denoisers (See **Fig. 1 (c)**), which could remove the pepper-and-salt noise and uniformly distributed noise in the images. The noised images firstly passed through the models forwardly to obtain the encoded patterns. Subsequently, the patterns propagated backwardly through the models to generate the denoised images. Additionally, we trained the models on noisy dataset (i.e., noisy input and clean target output) to enhance their denoising capability, resulting in the DSOAE and DMOAE models.

**Fig. 4 (a)** present the ability of these two models in eliminating pepper-and-salt noise through typical samples. The intensity of this type of noise is controlled by the parameter  $\alpha$  (See **Methods and Materials for detailed definition**). For SOAE model, the PSNR between reconstructed image and denoised images differs by less than 1.6 dB when  $\alpha$  is less than 0.5, resulting in high image clarity. The quality of denoised images will rapidly decrease as  $\alpha$  increases from 0.5 to 0.7, with PSNR of around 16 dB at  $\alpha = 0.7$ .  $\eta_F$  also decreases from around 70% to around 28% with the increase of  $\alpha$ , which is because the removed noise carried significant energy, meaning that the denoising process primarily occurred during the forward transmission. This indicates that our model can extract useful latent space information from noisy inputs. The denoising behavior of the MOAE model aligns with that of the SOAE model, with both PSNR and  $\eta_F$  decreasing as noise intensity increases. The performance of models on removing uniformly distributed noise is demonstrated in **Fig. 4 (b)**. Parameter  $\beta$  determines the noise intensity (See **Methods and Materials for detailed definition**). The SOAE model and MOAE model can also eliminate this kind of noise following the analysis of pepper-and-salt noise. Moreover, the four additionally trained DMOAE and DSOAE models can effectively enhance the denoising image clarities and the system efficiencies. By comparison, High-intensity noise will add extra background to images processed by the SOAE model and cause images handled by the MOAE model to become blurred. Uniformly distributed noise has a weaker impact on image contours compared to verification noise.

**Fig. 4 (c)** illustrates the PSNR histograms of noisy and denoised MNIST validation sets. The median PSNR of the dataset affected by pepper-and-salt noise is 7.81 dB. This value improves significantly to 17.3 dB with the SOAE model and further increases to 18.6 dB using the DSOAE model. The MOAE and DMOAE denoisers respectively enhance the median to 14.4 dB and 14.8 dB. Uniformly distributed noise has a milder interference effect on the images, resulting in a higher median PSNR of 9.94 dB. After processing with the SOAE, DSOAE, MOAE, and DMOAE models, the median PSNR increases to 14 dB, 19 dB, 14.2 dB, and 14.9 dB, respectively. **Fig. 4 (d)** reflects the impact of noise intensity on PSNR and transmission efficiency (average value). By comparing PNSR curves in the four plots and median values of **Fig. 4 (c)**, we can conclude that the SOAE model's ability to remove uniformly distributed noise is weaker than its capacity to eliminate pepper-and-salt noise. However, the DSOAE model effectively compensates for this shortcoming, significantly enhancing the model's denoising capability for the former. The MOAE and DMOAE models perform comparably for both types of noise. Moreover, the maximum PSNR improvement of 10.89 dB is achieved by the DSOAE model at  $\alpha = 0.6$ .  $\eta_F$  of the four models decrease with increasing noise intensity, consistent with above regulation, but their  $\eta_B$  changes relatively slightly. It is also noteworthy that the SOAE and DSOAE denoisers have external generalization ability, which is illustrated in **Supplementary Fig. S6**.

## Application 2: Image classification

Next, reconfigurable image classifiers were constructed using encoders from well-trained OAE basic models and pluggable phase-only diffractive layers. The encoders with fixed phase profiles functioned as feature extractors, while the pluggable layers, optimized through training, served for classification (See **Fig. 1 (c)**). These mechanically reconfigurable classifiers can be trained to handle various datasets by inserting different classification layers after the same encoder. Benefiting from the denoising capability of the encoders (See **Application 1**), our classifiers also exhibited strong noise resistance, thus we referred to them as noise-resistant reconfigurable image classifiers (NRICs). For convenience, we denote the combination of feature extractors and classification layers using model and dataset names. One example is the SMNIST-1EMNIST NRIC, which represents a classifier trained on EMNIST for classification, including a well-trained SOAE feature extractor from the MNIST dataset

and one classification layer.

**Fig. 5 (a)** shows the classification performance and phase profiles of the SMNIST-1MNIST, SMNIST-1EMNIST, and SMNIST-1Fashion NRICs. The accuracies of the first two classifiers are close, being 84.6% and 84.1%, respectively. And their system efficiencies are both 1.3%. The third classifier has the lowest accuracy and efficiency, at 73.2% and 1.1%, respectively, due to smaller inter-class differences in the Fashion dataset. **Fig. 5 (b)** presents the results for SMNIST-2MNIST, SMNIST-2EMNIST, and SMNIST-2Fashion NRICs. The accuracies of these classifiers are improved by approximately 4.5% with the addition of an extra classification layer, reaching 89.7%, 88.1%, and 77.7%, respectively. Meanwhile, the system efficiencies increase to 2.5%, 2.5%, and 1.8%. The classification performances of six NRICs based on the MOAE encoder are displayed in **Fig. 5 (c)** and **(d)**, and they are similar to the performances of corresponding classifiers mentioned above. **Fig. 5 (e)** presents the accuracies of all 36 types of NRICs. The highest accuracies achieved on the MNIST, EMNIST, and Fashion datasets are 89.8%, 88.7%, and 78.4%, respectively, comparable to the accuracies of ordinary diffractive classifiers under the same configurations (See **Supplementary Fig. S8**). **Fig. 5 (f)** illustrates the impact of noise intensity on the accuracy of ordinary classifier, SMNIST-2MNIST, and MMNIST-2MNIST NRICs. When images are disturbed by salt-and-pepper noise with  $\alpha = 0.6$ , the NRIC maintains an accuracy above 81.5%, while that of ordinary classifier drops to 66.4%. With the increase of the noise intensity, the gaps between the curves get widened, which indicates that the accuracy of ordinary classifier declines more rapidly than the accuracies of NRICs. The NRICs demonstrate even greater resistance to uniformly distributed noise. At  $\beta = 0.6$ , the accuracies of NRICs are around 79%, while that of ordinary classifier plummets to only 18.9%.

### Application 3: Image generation

Finally, the decoders of SOAE and MOAE models were utilized to achieve hologram generations (HGs) and conditional hologram generations (CHGs, See **Fig. 1 (c)**). For HG, the pre-obtained encoded patterns of original images were directly taken as input patterns for the generators to project holograms. In contrast, for CHG, the generators created holograms utilizing any patterns, with their categories being determined by the positions of the input patterns. **Fig. 6 (a)** illustrates the HGs on MNIST, EMNIST and Fashion datasets. Specifically, we used the average of the encoded patterns for each class of original images as the input patterns. Due to the convex lens-like characteristics of SOAE models trained on MNIST and EMNIST, input patterns of their generators are actually the average down-scaled images of original images, which are then enlarged to generate holograms. Instead, the SOAE generator trained on Fashion dataset and three MOAE generators produce holograms from average encrypted encoded patterns. The generated holograms clearly display the typical features of each category of images but the edges of some images are slightly blurred due to the averaging of multiple encoded patterns.

**Fig. (b)-(d)** represent the CHGs using MOAE generator trained on MNIST dataset. By respectively employing ten average encoded patterns at different places of each class as model inputs, image transformations, a specific situation of CHGs was implemented and illustrated in **Fig. (b)**. Each column of **Fig. (b)** presents the result of transforming one digit into other nine digits. The ten categories of images can be flexibly converted into one another by the MOAE generator, and the details of the same category of digits converted from different category digits vary (i.e., The width of 0, the curvature of 2, and the inclinations of 5 and 7). From the perspective of linear space, the ten encoding regions can be considered as the bases of the ten categories of images in the latent space and the pattern content can be thought as weight of each basis. The forward encoding process decomposes the non-orthogonal original images onto the ten bases in the latent space, while the image transformation process directly utilizes the components on each basis to generate the corresponding category images. **Fig. (c)** and **Fig. (d)** respectively show the CHGs from specific input patterns (constant, gaussian, cosine and sine) and random input patterns (normal distributions and uniform distributions). Even though these input patterns were not from the encoded patterns, images with unique categorical features were still generated and different patterns produced various image details. It is also noteworthy that the holograms in these two figures contain more noise than holograms in **Fig. (b)**, whose reasons and mitigation measures are detailed in **Discussion**. The results of CHGs indicate that a well-trained MOAE model can store the primary information of a dataset in its diffraction layer phase profiles, and input patterns can be utilized as indexes to extract the information. This could provide new insights for enhancing the channel capacity of hypersurface holography and optical storage.

### Validation of OAE framework and its applications

For the purpose of validation, we further trained tiny experimental models on sub-datasets and manufactured them utilizing 3D printing technology. The diffraction layers of the experimental models are composed of periodically arranged micropillars, with the transmission coefficient of each metaatom being modulated by the height of the micropillars (See **Methods and Materials** for detailed settings of experimental models, sub-datasets, 3D printer and materials). The encoding region of tiny SOAE and MOAE models are both a square with a side length of 8, resulting in a compression ratio of 16.

**Fig. 7 (a)** and **(b)** respectively illustrate the actual and conceptual experiment systems. A two-stage laser was used to generate 0.69 THz laser light, a Keplerian lens system was employed for beam shaping, and a THz camera was used to capture THz images (See **Methods and Materials**

for device details). **Fig. 7 (c)** presents the experimental verification results of the SOAE model trained on the MNIST subset and its denoising capability. For the convenience of fabrication, we simply binarized the numerically computed encoded patterns (4th column), which were then manufactured for the backward transmission (decoder) experiment. **Supplementary Fig. S11** further provide two practical designs to directly obtain denoised images through reflection. Due to quantization loss of the latent space patterns, the reconstructed images have slightly thicker lines than the original images. **Fig. 7 (d)** shows the verification of CHGs using MOAE generator trained on MNIST subset. The encoding regions distribution of experimental MOAE model can be found in **Supplementary Fig. S12**. This figure demonstrates that MOAE model can generate target numbers using constant input pattern at different positions. The height profiles of the tiny 2-layer SOAE and MOAE models are shown in **Fig. 7 (e)** and their metrics can be found in **Supplementary Fig. S13**.

**Fig. 7 (f)** validates the classification performance of MMNIST-1EMNIST, MMNIST-1MNIST, MMNIST-1Fashion NRICs. Due to limitations of the experimental platform (i.e., small illumination area of THz camera), we employed an RSC method (See **Methods and Materials**) that utilized fivefold upsampling of the original grids to validate the classification results. The energy distributions calculated by two methods match very well and the contrasts between maximum energy and second maximum energy are significant, which proofs recognition abilities of NRICs. The accuracies of the three models are respectively 89.8%, 92.0% and 89.4% (See **Supplementary Fig. S14**). Besides, we also trained a set of miniature models for CST simulation and their results are shown in **Supplementary Fig. S15**.

## Discussion

To analyze the impacts of parameters on SOAE model performance, we separately altered the depth (number of layers), the distance between adjacent layers, and the radius of the circular encoding region, while keeping all other parameters unchanged to observe the variation pattern of metrics. The variation relationship curves and the corresponding examples are respectively shown **Supplementary Fig. S16 (a)** and **(b)**. As the model depth increases, both the quality of the reconstructed images and the bidirectional transmission efficiency initially rise and then decline, reaching an optimal point at a depth of 5. The corresponding image examples also indicate that the model exhibits lens-like characteristics only when the depth is 5, resulting in the clearest images. When the depth is shallow, the images appear blurry, and when the depth is too deep, artifacts are introduced. At sufficiently large distances (greater than 2.32 cm), it has little effect on the model performance, indicating that the neurons in each layer have been fully connected. The variation trend of metrics with respect to the radius is consistent with that concerning depth, reaching optimal performance at a radius of 10. It can be seen from the example images that when the encoding radius exceeds 10, the model fails to learn the general imaging rules of a convex lens, resulting in a decline in performance.

Despite the amplitude of wavefield, our SOAE model can additionally use intensity or phase of wavefields to present the images in original space. The last row of **Supplementary Fig. S16 (a)** and **(b)** displays the metrics and examples of model using different properties to present images (i.e., ‘A-I’: Original images are carried on amplitude of light but reconstructed images are represented by intensity of light.). The image qualities of the ‘A-A’, ‘A-I’, ‘I-A’, ‘I-I’ modes are nearly equivalent, with an SSIM of approximately 0.87. The ‘I-A’ mode has the lowest value for  $\eta_F$ , while the ‘A-I’ mode has the lowest value for  $\eta_B$ . The metrics for the two phase-input modes are lower than those of the aforementioned four modes (SSIM  $\sim 0.7$ , PSNR  $\sim 15$  dB,  $\eta_F \sim 7\%$ , and  $\eta_B \sim 52\%$ ). However, they can achieve the conversion of phase information. It can be observed from the examples that the image of the ‘P-A’ mode is the bluriest, the image of the ‘I-I’ mode has the sharpest edges, and the image of the ‘I-A’ mode exhibits the least noise.

**Supplementary Fig. S16 (c)** illustrates impact of  $\eta_{Fth}$  and  $\eta_{Bth}$  on the performance of the MOAE model ( $\eta_{Bth} = 10\eta_{Fth}$ ). Due to the constraint imposed by the efficiency regularization term, increasing these two hyperparameters improves the bidirectional transmission efficiency of the system. However, this also leads to a decrease in image quality, causing the images to become blurry. Thus, the image quality and transmission efficiency of the MOAE model represent a trade-off that must be balanced.

In this article, we propose an OAE framework for all-optical machine learning. This framework fully exploits the bidirectional information channels of the D<sup>2</sup>NN, enabling it to function as both an optical encoder and decoder in two transmission directions using only a single set of diffractive layers, which enhances the system compactness and integration. By modifying prior shape distributions, various OAE models are developed to demonstrate the encoding and representation capabilities of the optical latent space. Two basic models, the SOAE and MOAE, both achieve compression encoding with an approximate compression ratio of 52. The SOAE model, utilizing a single encoding region, can learn the imaging principles of convex lenses through the reconstruction of MNIST or EMNIST datasets, which produces high-quality reconstructed images with an SSIM exceeding 0.85. This result showcases the potential of D<sup>2</sup>NNs to uncover general physical principles. In contrast, the MOAE model features multiple encoding regions located at different positions, each containing encrypted encoding information for a specific category. It demonstrates the spatial position encoding capability of the optical latent space. Additionally, six extended modes explore a variety of encoding patterns, further demonstrating that the latent space can flexibly encode raw information into regions of any shape.

The well-trained SOAE and MOAE models are employed to construct image denoisers, classifiers and generators. The dual modulation effect of each diffractive layer, combined with the spatial filtering effect of the compressed encoding in the latent space, enables our denoisers to achieve superior noise reduction performances compared to the unidirectional end-to-end diffractive denoisers<sup>39</sup> with the same number of layers. Additionally, our denoisers are capable of removing other types of noise, such as Gaussian noise and Rayleigh noise. By flexibly combining the independently trained encoder (feature extractor) with newly inserted classification layers, our classifiers can achieve classification across multiple datasets in a mechanically reconfigurable manner. Although only three datasets are used in this article, our classifiers can be simply extended to classify more datasets, such as Quickdraw and KMNIST, by inserting new classification layers for behind the encoder. Moreover, this assembly approach enables our classifiers to possess stronger noise resistance characteristics compared to conventional diffractive classifiers. Image generators achieve hologram generations and conditional hologram generations. The former directly produces holograms with large FOV from the encoded patterns in small regions, which can be used in AR or VR<sup>56</sup>. The latter projects different categories of images based on positions of input patterns. The conditional hologram generator indicates that a well-trained MOAE model can be regarded as a special memory that retains dataset information, with its index defined by the position and content of the input patterns. This will offer a new approach for enhancing the capacity of hypersurface holography and optical information storage<sup>57-60</sup>. Furthermore, the encrypted characteristics and shape-controllable features of the encoding patterns in the six extended modes make them promising candidates for optical image encryption and obstacle-avoiding optical communication<sup>52,61,62</sup>.

The OAE framework also exhibit certain limitations. Due to the energy loss of transmissive hypersurfaces, the reconstruction efficiency of systems requiring bidirectional transmission mechanisms (e.g., Image denoising) will significantly decrease with the additional transmissive modulation. Carefully-designed high-transmittance hypersurfaces<sup>63,64</sup> can help improve system efficiency to a certain extent. Besides, the input and output FOV of bidirectional transmission system are same, which hinders the measurement of output results. We illustrate two practical designs using beam splitters or off-axis imaging in **Supplementary Fig. S11** to solve the problem. As for the CHGs, the holograms generated by the specific function patterns and random patterns are blurred. There are two reasons for this phenomenon. For one thing, our MOAE model can only perform linear operations. While it can separate different categories of images through positional encoding, it struggles to effectively track significant variations within the same category, resulting in only the average output of those images. For another, the content of the encoding patterns for each category lacks a prior distribution, which prevents us from providing the generator with an encoding pattern containing accurate image information. To achieve controllable and clear conditional hologram generation, we can design an optoelectronic hybrid model composed of a nonlinear electronic encoder and a nonlinear D<sup>2</sup>NN<sup>30</sup> generator and train it using the loss function containing positional encoding and prior distribution regularization term. Finally, to ensure the accuracy of numerical calculations, the lateral dimensions of our units are all greater than or equal to one  $\lambda$ , which limits the miniaturization of models. By using error compensation methods such as zero-padding<sup>55</sup>, the unit size can be reduced to approximately  $\lambda/2$ , which is the diffraction limit.

In summary, our OAE framework explores new dimensions of optical encoding in shape encoding and positional encoding, characterized by compactness and multifunctional integration. It can be applied in various fields such as pattern recognition, image processing, computational holography, optical storage, optical communication, and optical image encryption, and is expected to promote the development of general intelligent optical systems.

## Methods and Materials

### Numerical propagation model for diffractive processors

The diffractive processor comprised an input layer, a set of diffractive layers and an output layer, each of which respectively located at a different axial position  $z_l$  ( $l = 0, 1, 2, \dots, N, N + 1$ ). The input wavefield can be modulated layer by layer when propagating from input plane ( $z_0$ ) to output plane ( $z_{N+1}$ ). Modulation effect of the  $l$  th layer ( $1 \leq l \leq N$ ) was expressed as follows:

$$\begin{aligned} U_l^o(x, y) &= U_l^i(x, y)T_l(x, y) \\ T_l(x, y) &= a_l(x, y) \exp(j\phi_l(x, y)) \end{aligned} \quad (1)$$

where  $U_l^i(x, y)$  and  $U_l^o(x, y)$  respectively represent input and output wavefield of the  $l$  th layer.  $T_l(x, y)$  is transmission coefficient of  $l$  th layer.

Propagation process between the  $l$  th layer and the  $l + 1$  th layer ( $0 \leq l \leq N$ ) can be described by the Rayleigh Sommerfeld convolution formula (RSC)<sup>55</sup> as follows:

$$\begin{aligned} U_{l+1}^i(x, y) &= U_l^o(x, y) * W(x, y, d_l) \\ d_l &= z_{l+1} - z_l \\ W(x, y, d_l) &= \frac{d_l}{r^2} \left( \frac{1}{2\pi r} + \frac{1}{j\lambda} \right) \exp(j \frac{2\pi r}{\lambda}) \end{aligned}$$

$$r = \sqrt{x^2 + y^2 + d_l^2} \quad (2)$$

where  $d_l$  is the distance between two layers, and  $W(x, y, d_l)$  is the convolution operator that reflects the diffraction connection of two layers.

Even though the RSC method was accurate enough to describe the diffraction process between two layers, the overlarge computational effort caused by large-kernel convolution made it impossible to be used in the training procedure. Therefore, we only used this method for numerical validation. Instead, a lower-computing and faster algorithm called angular spectrum method (ASM) was utilized for model training and inference, which can be expressed as follows:

$$\begin{aligned} U_{l+1}^i(x, y) &= \text{IFFT}(\text{FFT}(U_l^o(x, y))H(f_x, f_y, d_l)) \\ H(f_x, f_y, d_l) &= \exp\left(\frac{j2\pi d_l}{\lambda}\sqrt{1 - (\lambda f_x)^2 - (\lambda f_y)^2}\right) \end{aligned} \quad (3)$$

where  $H(f_x, f_y, d_l)$  is the spectrum transfer function,  $f_x$  and  $f_y$  are spatial frequencies along x and y axis, respectively.

### Loss functions and metrics

In our work, The OAE models function as encoders when input images pass through them in the forward direction ( $FOV_I \rightarrow FOV_{II}$ ). Conversely, they act as decoders when the encoded patterns pass through in the backward direction ( $FOV_{II} \rightarrow FOV_I$ ). We wrote the Loss function for training OAE models as follows:

$$\mathcal{L}_{OAE} = \mathcal{L}_{Rec} + \gamma_{En}\mathcal{L}_{En} + \gamma_{Eff}\mathcal{L}_{Eff} \quad (4)$$

Here,  $\mathcal{L}_{Rec}$  represents the reconstruction error between input images and corresponding decoded images, and is defined as:

$$\begin{aligned} \mathcal{L}_{Rec} &= \mathcal{L}_{MSE}(I(x, y), O_{De}(x, y)) = E[|\sigma_1 I(x, y) - \sigma_2 O_{De}(x, y)|^2] \\ \sigma_1 &= \frac{1}{\sum_{(x,y) \in FOV_I} I(x, y)} \\ \sigma_2 &= \sigma_1 \frac{\sum_{(x,y) \in FOV_I} I(x, y) O_{De}(x, y)}{\sum_{(x,y) \in FOV_I} |O_{De}(x, y)|^2} \end{aligned} \quad (5)$$

where  $E[\cdot]$  is the average operator,  $I(x, y)$  stands input image and  $O_{De}(x, y)$  stands decoded image.  $\sigma_1$  and  $\sigma_2$  are parameters that eliminate the error due to diffractive energy loss.

$\mathcal{L}_{En}$  is a regularization term designed to maximize the concentration of energy in the target encoding region, which can be expressed as:

$$\begin{aligned} \mathcal{L}_{En} &= -\ln\left(\frac{\sum_{(x,y) \in FOV_{II}} |M(x, y) O_{En}(x, y)|^2}{\sum_{(x,y) \in FOV_{II}} |O_{En}(x, y)|^2}\right) \\ M(x, y) &= \begin{cases} 1, & (x, y) \in \text{encoding region} \\ 0, & \text{otherwise} \end{cases} \end{aligned} \quad (6)$$

where  $O_{En}(x, y)$  represents the encoder output in  $FOV_{II}$ .  $M(x, y)$ , a region mask function that defines the shape of encoding patterns, guides the output to align with the target shape by providing a prior shape distribution, similar to the prior probability distribution in the electronic VAE model.

$\mathcal{L}_{Eff}$  is another regulation term that controls the bidirectional diffraction efficiency. For SOAE and its extended models, we simply used the reconstruction efficiency to constrain the model weights. The equation can be expressed as follows:

$$\begin{aligned} \mathcal{L}_{Eff} &= \begin{cases} -\ln\left(\frac{\eta_R}{\eta_{Th}}\right), & \eta_R < \eta_{Th} \\ 0, & \eta_R \geq \eta_{Th} \end{cases} \\ \eta_R &= \frac{\sum_{(x,y) \in FOV_I} |O_{De}(x, y)|^2}{\sum_{(x,y) \in FOV_I} |I(x, y)|^2} \end{aligned} \quad (7)$$

In the MOAE model, both forward and backward efficiency were used to more accurately regulate the bidirectional efficiency, as expressed below:

$$\begin{aligned} \mathcal{L}_{Eff} &= \begin{cases} -\ln\left(\frac{\eta_F}{\eta_{Fth}}\right), & \eta_F < \eta_{ThF} \\ 0, & \eta_F \geq \eta_{ThF} \end{cases} + \begin{cases} -\ln\left(\frac{\eta_B}{\eta_{Bth}}\right), & \eta_B < \eta_{ThB} \\ 0, & \eta_B \geq \eta_{ThB} \end{cases} \\ \eta_F &= \frac{\sum_{(x,y) \in FOV_{II}} |M(x, y) O_{En}(x, y)|^2}{\sum_{(x,y) \in FOV_I} |I(x, y)|^2}, \quad \eta_B = \frac{\sum_{(x,y) \in FOV_I} |O_{De}(x, y)|^2}{\sum_{(x,y) \in FOV_{II}} |M(x, y) O_{En}(x, y)|^2} \end{aligned} \quad (8)$$

$\eta_{Th}$ ,  $\eta_{ThF}$  and  $\eta_{ThB}$  are hyperparameters that control the total, forward, and backward efficiencies, respectively. Similarly,  $\gamma_{En}$  and  $\gamma_{Eff}$  in equation (4) are hyperparameters representing the weight coefficients for the encoding shape and efficiency penalty terms.

Moreover, The encoders ( $FOV_I \rightarrow FOV_{II}$ ) from trained SOAE and MOAE models were further utilized for classification. They were taken

as generalized feature extractors, capturing compact information from input images. By cascading one or two to-be-trained diffractive layers behind the fixed encoders, we implement  $\mathcal{L}_{\text{NRIC}}$  using  $\mathcal{L}_{\text{MSE}}$  in equation (5) to train image classifiers. The formula of  $\mathcal{L}_{\text{RLC}}$  was as follows:

$$\mathcal{L}_{\text{NRIC}} = \mathcal{L}_{\text{MSE}}(S(x, y), O_{\text{NRIC}}(x, y)) \quad (9)$$

where  $S(x, y)$  represents the focus pattern associated with the input class (i.e., See **Supplementary Fig. S11**),  $O_{\text{NRIC}}(x, y)$  denotes the output wavefield of classifier.

In addition to the above-mentioned MSE and efficiency ( $\eta$ ), we also used two additional metrics: Structural Similarity Index (SSIM) and Peak Signal-to-Noise Ratio (PSNR), to comprehensively evaluate the performance of the trained models. SSIM measured the similarity between images based on brightness, contrast, and structure, and can be expressed as follows:

$$SSIM = \frac{(2E[I(x, y)] + C_1)(2\text{Cov}[I(x, y), O_{\text{De}}(x, y)] + C_2)}{(E[I(x, y)]^2 + E[O_{\text{De}}(x, y)]^2 + C_1)(\text{Var}[I(x, y)] + \text{Var}[O_{\text{De}}(x, y)] + C_2)} \quad (12)$$

Here,  $\text{Cov}[\cdot, \cdot]$  calculates the covariance between two images, while  $\text{Var}[\cdot]$  represents the variance of an image. To more accurately assess similarity, we divided the two images into multiple blocks of size  $W \times W$  and compute the average SSIM across these blocks as the final results.

PSNR quantified the noise in the reconstructed image compared to the original image and can be expressed as follows:

$$PSNR = 10\log_{10} \frac{1}{E[\|\tilde{I}(x, y) - \tilde{O}_{\text{De}}(x, y)\|^2]} \quad (13)$$

where  $\tilde{\cdot}$  is normalization operator.

### Image noise models

The well-trained OAE and DOAE models were utilized to eliminate two common types of noise in images, specifically, salt-and-pepper noise and uniformly distributed noise. Salt-and-pepper noise appeared as randomly distributed black and white pixels in an image, creating a noticeable speckled effect. It was introduced to the original image according to the following formula:

$$I_{\text{noised}}^{\text{Pepper}}(x, y) = \begin{cases} 0, & (x, y) \in \text{Pepper region} \\ 1, & (x, y) \in \text{Salt region} \\ I(x, y), & \text{otherwise} \end{cases} \quad (10)$$

The noise intensity was controlled by the parameter  $\alpha$ . Specifically, randomly selected pixels in the pepper region and those in the salt region each accounted for  $\alpha/2$  of the total pixels. Uniformly distributed noise manifested as random perturbations on the original pixels, giving the image a grainy texture. It was added to the original image in the following way:

$$I_{\text{noised}}^{\text{Uniform}}(x, y) = I(x, y) + U(x, y) * \beta * E[|I(x, y)|^2] \quad (11)$$

where each pixel of  $U(x, y)$  follows a uniform distribution between 0 and 1 ( $\text{Y}(0,1)$ ). Parameter  $\beta$  determines the uniformly distributed noise intensity.

### Parameter details of diffractive processors

For the numerical implementation of all diffractive processors in our work (i.e., the SOAE model and its extensions, the MOAE model, DSOAE/DMOAE model, NRIC model, and HG/CHG model), we set the transmission coefficient as following equation:

$$\begin{aligned} a_l(x, y) &= 1 \\ \phi_l(x, y) &= 2\pi \text{Sigmoid}(\phi'_l(x, y)) \end{aligned} \quad (12)$$

where  $\phi'_l(x, y)$  is the only trainable parameter. The sample period, also the cell interval, of these numerical models was 0.435 mm (i.e.,  $\lambda = 0.435$  mm for  $f_0 = 0.69$  THz).  $FOV_I$  and  $FOV_{II}$  were both 27.84 mm  $\times$  27.84 mm in size (64\*64 pixels). The diffractive layer sets of numerical models were all 69.6 mm  $\times$  69.6 mm in size (160 \* 160 pixels) and distances between two successive layers,  $d_l$ , were all 34.8mm (80 $\lambda$ ). During the training process, parameter choices of loss functions would significantly determine the model performance. We elaborately designed these parameters for different models as follows.  $\gamma_{En}$  and  $\gamma_{Eff}$  in equation (4) for training SOAE model and its extensions, as well as DSOAE model were respectively set to 5e-5 and 0.1, with  $\eta_{Th}$  in equation (7) being 4%. For the MOAE and DMOAE models,  $\gamma_{En}$  was defined as 0, while  $\gamma_{Eff}$  was specified as 0.3.  $\eta_{Fth}$  and  $\eta_{Bth}$  in equation (8) were respectively 2% and 20%. The standard MNIST and Fashion-MNIST datasets, along with a subset of the EMNIST dataset, were used to train these numerical models. From the full 36-class EMNIST dataset, we selected 10 different letters, assigning 5,400 images to the training set and 900 images to the validation set for each class.

To validate the numerical models, diffractive layers consisted of thousands of micro pillars were fabricated using 3D printing technology. These layers were used to construct the SOAE, NRIC, and CHG models. The transmission coefficient of each pillar was modeled as follows:

$$a_l(x, y) = \exp\left(\frac{-2\pi k(\lambda)h_l(x, y)}{\lambda}\right)$$

$$\phi_l(x, y) = (n(\lambda) - 1) \frac{2\pi h_l(x, y)}{\lambda}$$

$$h_l(x, y) = \text{Sigmoid}(h'_l(x, y))(h_m - h_b) + h_b \quad (13)$$

Here,  $n(\lambda)$  and  $k(\lambda)$  represent refractive index and extinction coefficient of 3D printing material, respectively, where  $n(\lambda)$  is 1.73 and  $k(\lambda)$  is 0.43.  $h_l(x, y)$  denotes the pillar height distribution of  $l$  th layer, with  $h'_l(x, y)$  as the trainable parameter.  $h_m$  and  $h_b$  controlo the maximum and minimum pillar heights, set to 1.1 mm and 0.5 mm, respectively. Each pillar had a lateral size of 0.55 mm ( $\sim 1.26 \lambda$ ). Both  $FOV_I$  and  $FOV_{II}$  measured 17.6 mm  $\times$  17.6 mm, with a resolution of 32\*32 pixels. Each experimental diffractive layer spanned 77 mm  $\times$  77 mm (140 \* 140 pixels), and the  $d_l$  was assigned to 50mm ( $\sim 115\lambda$ ). The loss function parameters  $\gamma_{En}$  and  $\gamma_{Eff}$  were configured identically to those in the previously described numerical models. However,  $\eta_{Th}$  was assigned as 0.25%, while  $\eta_{Fth}$  and  $\eta_{Bth}$  were 0.5% and 5%, respectively. The datasets for the experimental models were subsets of the three datasets mentioned above, created by selecting 5 classes from the original 10 in each.

The diffractive models in our work were implemented using Python and PyTorch on a workstation equipped with a Xeon® Gold 6430 CPU and a GeForce RTX 4090 GPU. During each training iteration, a mini-batch composed of 128 randomly selected images was input to the model. After calculating the loss for one mini-batch, the Adam optimizer with a learning rate of 0.01 was used to perform backpropagation (BP) and update the trainable parameters. The number of epochs was set between 100 and 300 for different models to ensure adequate optimization.

### Experimental set-up

For our proof-of-concept experiments, we utilized a PolyJet 3D printer with 0.1 mm accuracy and 0.014 mm z-axis resolution to fabricate both diffractive layers and test objects. The 3D printer produced compact pillars of varying heights, which were assembled to form the diffractive layers. The test objects were designed with hollow patterns to encode information into the amplitude of the input wavefield and were then coated with aluminum foil to block surrounding waves. The complete set of diffractive processor was secured in a slot, which was fabricated using an SLA 3D printer with 0.1 mm accuracy.

To stimulate our diffractive processors, we used a FIRL-100 terahertz laser, as shown in the schematic in **Fig. 7(b)**. This system generated 70 mW of light at 0.69 THz. The FIRL-100 integrates both the CO2 pump laser (PL5) and the FIR laser (295-FIR) into a single compact unit, combining an efficient optically pumped FIR system. The CO2 section produces 80 lines within the wavelength range of 9.1  $\mu\text{m}$  to 10.9  $\mu\text{m}$ , utilizing a flowing gas single discharge tube that delivers over 50 W output on its strongest lines. The output from this section is coupled into the FIR laser, which is filled with CH3OH molecules, via two steering mirrors and a ZnSe focusing lens. When the 9R20 CO2 pump line is selected by tuning the resonator, the CH3OH molecules in the FIR laser are stimulated to produce 0.69 THz light with a 10 mm  $\times$  10 mm aperture. Following the light emission, we employed a Keplerian convex lens system to either magnify the light aperture by 4 times for encoder input or reduce it by 4 times for decoder input.

At the imaging plane, a THz camera (RIGI) with a resolution of 120  $\times$  160 pixels and a pixel size of 25  $\mu\text{m}$  was mounted on an XYZ three-axis motion stage. During the experiment, the camera was shifted along the Y/Z axes to capture the entire image. Depending on the pattern size, the camera was moved 1\*2, 3\*3, or 4\*5 times. Since the camera records only relative intensity in each frame, we first normalized the camera data by using the maximum intensity of each block from the numerical results. The individual blocks were then assembled and averaged to form the complete image, with an averaging step of every 22 pixels.

Furthermore, aim to mitigate experimental error, we specifically consider two principal sources of error caused by inadequate 3D printing accuracy: the axial displacement error and the height error of the diffractive layer pillars. Axial displacement error will make the pattern on the original focal plane defocused and blurred. It is incorporated by adding random bias ( $B_z \sim \mathcal{Y}(-\Delta z, \Delta z)$ ) to the distance between adjacent diffractive layers during the training process, where  $\Delta z$  is set to 0.5 mm. Pillar height errors distort the transmission coefficients, leading to noise artifacts in the focal plane. Therefore, Gaussian noise ( $\Delta h \sim \mathcal{N}(0, \delta/3)$ ), given the three-sigma rule of Gaussian distribution, is added to the height of each cell during training. Here,  $\delta$  represents accuracy of 3D printing and set to 0.1 mm.

### ACKNOWLEDGMENT

The authors acknowledge the financial support by the National Natural Science Foundation of China (Grants No.61991423).

### REFERENCES

1. Tu, Z. et al. MAXIM: Multi-Axis MLP for Image Processing. In *Proceedings of the 2022 IEEE/CVF Conference on Computer Vision and Pattern Recognition*. 5759-5770 (IEEE, 2022)

2. Valsesia, D., Fracastoro, G. & Magli, E. Deep Graph-Convolutional Image Denoising. *IEEE Trans. Image Process.* **29**, 8226-8237, 10.1109/TIP.2020.3013166 (2020)
3. Devlin, J. et al. BERT: Pre-training of Deep Bidirectional Transformers for Language Understanding. In *Proceedings of the 2019 Conference of the North American Chapter of the Association for Computational Linguistics: Human Language Technologies*. 4171–4186 (ACL, 2018)
4. Xie, S. et al. Aggregated Residual Transformations for Deep Neural Networks. In *Proceedings of the 2017 IEEE Conference on Computer Vision and Pattern Recognition*. 5987-5995 (IEEE, 2017)
5. Wang, C. Y., Bochkovskiy, A. & Liao, H. Y. M. YOLOv7: Trainable Bag-of-Freebies Sets New State-of-the-Art for Real-Time Object Detectors. In *Proceedings of the 2023 IEEE/CVF Conference on Computer Vision and Pattern Recognition*. 7464-7475 (IEEE, 2023)
6. Jiang, J., Chen, M. & Fan, J. A. Deep neural networks for the evaluation and design of photonic devices. *Nat. Rev. Mater.* **6**, 679-700, <https://doi.org/10.1038/s41578-020-00260-1> (2021)
7. Liu, Z. et al. KAN: Kolmogorov-Arnold Networks. Preprint at <https://doi.org/10.48550/arXiv.2404.19756> (2024)
8. Brown, T. B. et al. Language Models are Few-Shot Learners. Preprint at <https://doi.org/10.48550/arXiv.2005.14165> (2020)
9. Michelucci, U. An Introduction to Autoencoders. Preprint at <https://doi.org/10.48550/arXiv.2201.03898> (2022)
10. Richardson, E. et al. Encoding in Style: a StyleGAN Encoder for Image-to-Image Translation. In *Proceedings of the 2021 IEEE/CVF Conference on Computer Vision and Pattern Recognition*. 2287-2296 (IEEE, 2021)
11. Vaswani, A. et al. Attention is all you need. In *Proceedings of the 31st International Conference on Neural Information Processing Systems*. 6000-6010 (ACM, 2017)
12. Zou, Z. et al. Stylized Neural Painting. In *Proceedings of the 2021 IEEE/CVF Conference on Computer Vision and Pattern Recognition*. 15684-15693 (IEEE, 2021)
13. Hofmann, V. et al. AI generates covertly racist decisions about people based on their dialect. *Nature*. **633**, 147-154, <https://doi.org/10.1038/s41586-024-07856-5> (2024)
14. Chen, X. et al. A neural speech decoding framework leveraging deep learning and speech synthesis. *Nat. Mach. Intell.* **6**, 467-480, <https://doi.org/10.1038/s42256-024-00824-8> (2024)
15. Markram, H. The Blue Brain Project. *Nat. Rev. Neurosci.* **7**, 153-160, <https://doi.org/10.1038/nrn1848> (2006)
16. Conti, S. Analogue chips for energy-efficient AI. *Nat. Electron.* **6**, 644-644, <https://doi.org/10.1038/s41928-023-01035-6> (2023)
17. Shen, Y. et al. Deep learning with coherent nanophotonic circuits. *Nat. Photonics*. **11**, 441-446, <https://doi.org/10.1038/nphoton.2017.93> (2017)
18. Feldmann, J. et al. Parallel convolutional processing using an integrated photonic tensor core. *Nature*. **589**, 52-58, <https://doi.org/10.1038/s41586-020-03070-1> (2021)
19. Liu, J. et al. Research progress in optical neural networks: theory, applications and developments. *PhotoniX*. **2**, 5, <https://doi.org/10.1186/s43074-021-00026-0> (2021)
20. Xu, X. et al. 11 TOPS photonic convolutional accelerator for optical neural networks. *Nature*. **589**, 44-51, <https://doi.org/10.1038/s41586-020-03063-0> (2021)
21. Xu, Z. et al. Large-scale photonic chiplet Taichi empowers 160-TOPS/W artificial general intelligence. *Science*. **384**, 202-209, <https://doi.org/10.1126/science.adl1203> (2024)
22. Fu, T. et al. Optical neural networks: progress and challenges. *Light Sci. Appl.* **13**, 263, <https://doi.org/10.1038/s41377-024-01590-3> (2024)
23. Lin, X. et al. All-optical machine learning using diffractive deep neural networks. *Science* **361**, 1004-1008, <https://doi.org/10.1126/science.aat8084> (2018)
24. Chong, M. et al. Generation of polarization-multiplexed terahertz orbital angular momentum combs via all-silicon metasurfaces. *Light.: Adv. Manuf.* **5**, 38, <https://doi.org/10.37188/lam.2024.038> (2024)
25. Hu, J. et al. Diffractive optical computing in free space. *Nat. Commun.* **15**, 1525, <https://doi.org/10.1038/s41467-024-45982-w> (2024)
26. Duan, Z., Chen, H. & Lin, X. Optical multi-task learning using multi-wavelength diffractive deep neural networks. *Nanophotonics*. **12**, 893-903, <https://doi.org/10.1515/nanoph-2022-0615> (2023)
27. Li, J. et al. Class-specific differential detection in diffractive optical neural networks improves inference accuracy. *Adv. Photonics*. **1**, 046001 - 046001, (2019)
28. Rahman, M. S. S. et al. Ensemble learning of diffractive optical networks. *Light Sci. Appl.* **10**, 14, <https://doi.org/10.1038/s41377-020-00446-w> (2021)
29. Wang, Z. et al. Integrated photonic metasystem for image classifications at telecommunication wavelength. *Nat. Commun.* **13**, 2131,

https://doi.org/10.1038/s41467-022-29856-7 (2022)

- 30. Zhou, T. et al. Large-scale neuromorphic optoelectronic computing with a reconfigurable diffractive processing unit. *Nat. Photonics.* **15**, 367-373, https://doi.org/10.1038/s41566-021-00796-w (2021)
- 31. Chen, H. et al. Diffractive Deep Neural Networks at Visible Wavelengths. *Engineering.* **7**, 1483-1491, https://doi.org/https://doi.org/10.1016/j.eng.2020.07.032 (2021)
- 32. Liu, Z. et al. Broadband, Low-Crosstalk, and Massive-Channels OAM Modes De/Multiplexing Based on Optical Diffraction Neural Network. *Laser Photon. Rev.* **17**, 2200536, https://doi.org/https://doi.org/10.1002/lpor.202200536 (2023)
- 33. Huang, M. et al. Diffraction Neural Network for Multi-Source Information of Arrival Sensing. *Laser Photon. Rev.* **17**, 2300202, https://doi.org/https://doi.org/10.1002/lpor.202300202 (2023)
- 34. Gao, S. et al. Super-resolution diffractive neural network for all-optical direction of arrival estimation beyond diffraction limits. *Light Sci. Appl.* **13**, 161, https://doi.org/10.1038/s41377-024-01511-4 (2024)
- 35. Kulce, O. et al. All-optical synthesis of an arbitrary linear transformation using diffractive surfaces. *Light Sci. Appl.* **10**, 196, https://doi.org/10.1038/s41377-021-00623-5 (2021)
- 36. Rahman, M. S. S. et al. Universal linear intensity transformations using spatially incoherent diffractive processors. *Light Sci. Appl.* **12**, 195, https://doi.org/10.1038/s41377-023-01234-y (2023)
- 37. Ding, X. et al. Metasurface-Based Optical Logic Operators Driven by Diffractive Neural Networks. *Adv. Mater.* **36**, 2308993, https://doi.org/https://doi.org/10.1002/adma.202308993 (2024)
- 38. Zhao, Z. et al. Deep learning-enabled compact optical trigonometric operator with metasurface. *PhotoniX.* **3**, 15, https://doi.org/10.1186/s43074-022-00062-4 (2022)
- 39. İşil, Ç. et al. All-optical image denoising using a diffractive visual processor. *Light Sci. Appl.* **13**, 43, https://doi.org/10.1038/s41377-024-01385-6 (2024)
- 40. Li, J. et al. Unidirectional imaging using deep learning–designed materials. *Sci. Adv.* **9**, eadg1505, https://doi.org/doi:10.1126/sciadv.adg1505 (2023)
- 41. Bai, B. et al. Pyramid diffractive optical networks for unidirectional image magnification and demagnification. *Light Sci. Appl.* **13**, 178, https://doi.org/10.1038/s41377-024-01543-w (2024)
- 42. Hu, J. et al. Subwavelength imaging using a solid-immersion diffractive optical processor. *eLight.* **4**, 8, https://doi.org/10.1186/s43593-024-00067-5 (2024)
- 43. İşil, Ç. et al. Super-resolution image display using diffractive decoders. *Sci. Adv.* **8**, eadd3433, https://doi.org/doi:10.1126/sciadv.add3433 (2022)
- 44. Li, J. et al. Polarization multiplexed diffractive computing: all-optical implementation of a group of linear transformations through a polarization-encoded diffractive network. *Light Sci. Appl.* **11**, 153, https://doi.org/10.1038/s41377-022-00849-x (2022)
- 45. Wang, Y., Pang, C. & Qi, J. 3D Reconfigurable Vectorial Holography via a Dual-Layer Hybrid Metasurface Device. *Laser Photon. Rev.* **18**, 2300832, https://doi.org/https://doi.org/10.1002/lpor.202300832 (2024)
- 46. Wang, Y. et al. Matrix Diffractive Deep Neural Networks Merging Polarization into Meta-Devices. *Laser Photon. Rev.* **18**, 2300903, https://doi.org/https://doi.org/10.1002/lpor.202300903 (2024)
- 47. Luo, X. et al. Metasurface-enabled on-chip multiplexed diffractive neural networks in the visible. *Light Sci. Appl.* **11**, 158, https://doi.org/10.1038/s41377-022-00844-2 (2022)
- 48. He, C. et al. Pluggable multitask diffractive neural networks based on cascaded metasurfaces. *Opto-Electron. Adv.* **7**, 230005, https://doi.org/10.29026/oea.2024.230005 (2024)
- 49. Liu, C. et al. A programmable diffractive deep neural network based on a digital-coding metasurface array. *Nat. Electron.* **5**, 113-122, https://doi.org/10.1038/s41928-022-00719-9 (2022)
- 50. Fang, X. et al. Orbital angular momentum-mediated machine learning for high-accuracy mode-feature encoding. *Light Sci. Appl.* **13**, 49, https://doi.org/10.1038/s41377-024-01386-5 (2024)
- 51. Li, J. et al. Spectrally encoded single-pixel machine vision using diffractive networks. *Sci. Adv.* **7**, eabd7690, https://doi.org/10.1126/sciadv.abd7690 (2021)
- 52. Rahman, M. S. S. et al. Learning diffractive optical communication around arbitrary opaque occlusions. *Nat. Commun.* **14**, 6830, https://doi.org/10.1038/s41467-023-42556-0 (2023)
- 53. Chen, Y. et al. Photonic unsupervised learning variational autoencoder for high-throughput and low-latency image transmission. *Sci. Adv.* **9**, eadf8437, https://doi.org/10.1126/sciadv.adf8437 (2023)

54. Falconer, K. *Fractal Geometry: Mathematical Foundations and Applications* (Wiley, 2014)
55. Zhang, W. et al. Analysis of numerical diffraction calculation methods: from the perspective of phase space optics and the sampling theorem. *J. Opt. Soc. Am. A.* **37**, 1748-1766, <https://doi.org/10.1364/JOSAA.401908> (2020)
56. Frisoli, A. & Leonardis, D. Wearable haptics for virtual reality and beyond. *Nat. Rev. Electr.* <https://doi.org/10.1038/s44287-024-00089-8> (2024)
57. Li, L. et al. Electromagnetic reprogrammable coding-metasurface holograms. *Nat. Commun.* **8**, 197, <https://doi.org/10.1038/s41467-017-00164-9> (2017)
58. Li, X. et al. Code Division Multiplexing Inspired Dynamic Metasurface Holography. *Adv. Funct.* **31**, 2103326, <https://doi.org/https://doi.org/10.1002/adfm.202103326> (2021)
59. Wang, J. et al. Unlocking ultra-high holographic information capacity through nonorthogonal polarization multiplexing. *Nat. Commun.* **15**, 6284, <https://doi.org/10.1038/s41467-024-50586-5> (2024)
60. Horiuchi, N. Holography: Optical forces for data storage. *Nat. Photonics.* **10**, 621-621, <https://doi.org/10.1038/nphoton.2016.196> (2016)
61. Qu, G. et al. Reprogrammable meta-hologram for optical encryption. *Nat. Commun.* **11**, 5484, <https://doi.org/10.1038/s41467-020-19312-9> (2020)
62. Bai, B. et al. Data-Class-Specific All-Optical Transformations and Encryption. *Adv. Mater.* **35**, 2212091, <https://doi.org/https://doi.org/10.1002/adma.202212091> (2023)
63. He, Q. et al. High-Efficiency Metasurfaces: Principles, Realizations, and Applications. *Adv. Opt. Mater.* **6**, 1800415, <https://doi.org/https://doi.org/10.1002/adom.201800415> (2018)
64. Phan, T. et al. High-efficiency, large-area, topology-optimized metasurfaces. *Light Sci. Appl.* **8**, 48, <https://doi.org/10.1038/s41377-019-0159-5> (2019)

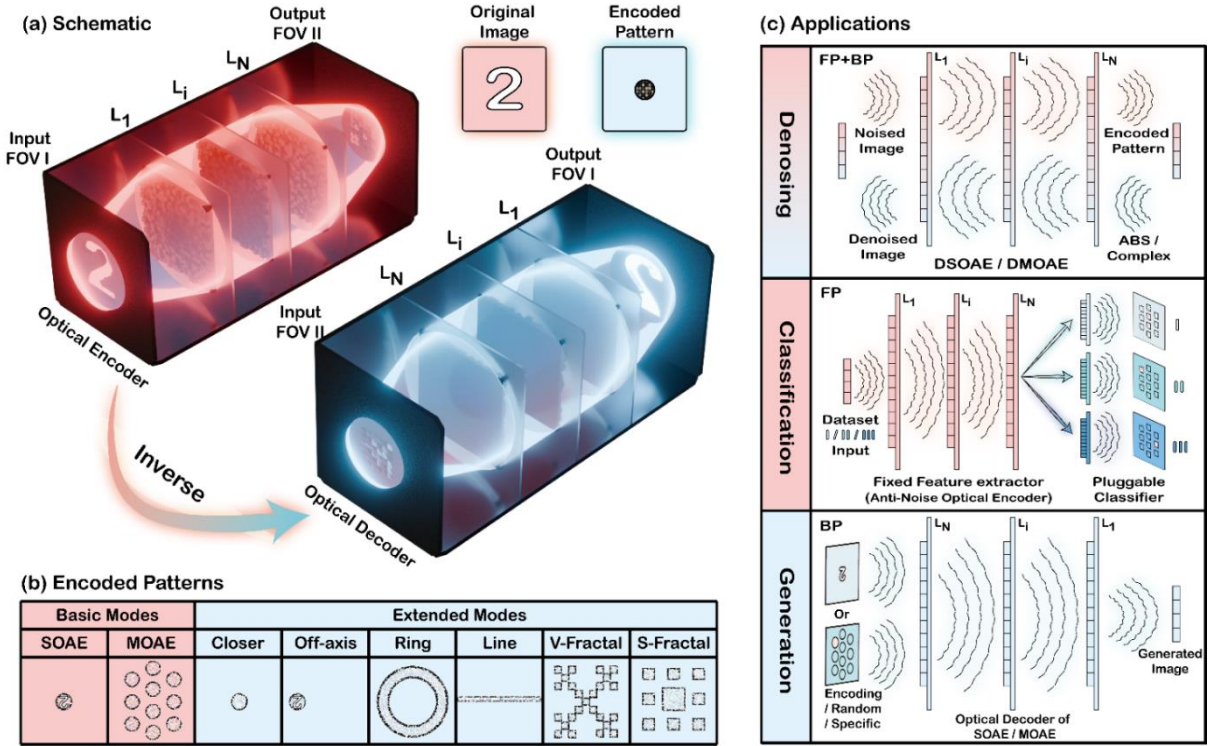


**Fig. 1 System schematic and applications of the all-optical autoencoder machine learning framework.** (a) System diagram of the OAE framework. It uses only one set of diffractive layers ( $L_1, \dots, L_i, \dots, L_N$ ) to separately implement the optical encoder and optical decoder in two directions. FOV: field of view.  $FOV_I \rightarrow FOV_{II}$  (Original image  $\rightarrow$  Encoded pattern): the optical encoder.  $FOV_{II} \rightarrow FOV_I$  (Encoded pattern  $\rightarrow$  Original image): the optical decoder. (b) Latent space encoding pattern design. The basic modes include SOAE and MOAE, which are further applied to three different scenarios. The extended modes explore six different encoded patterns in latent space. (i.e., Closer: Altering the distance between  $FOV_{II}$  and  $L_N$  closer. Off-axis: Moving encoded region bias from center. Ring: Making encoded pattern distribute in a ring. Line: Arranging encoded pattern along the line in a one-dimensional order. V-Fractal and S-Fractal: Designing the shape of encoded region as Vicsek and Sierpinski carpet fractal) (c) Three applications of the SOAE and MOAE models: image denoising (bidirectional transmission), noise-resistant reconfigurable image classification ( $FOV_I \rightarrow FOV_{II}$ ), and hologram generation ( $FOV_{II} \rightarrow FOV_I$ ).

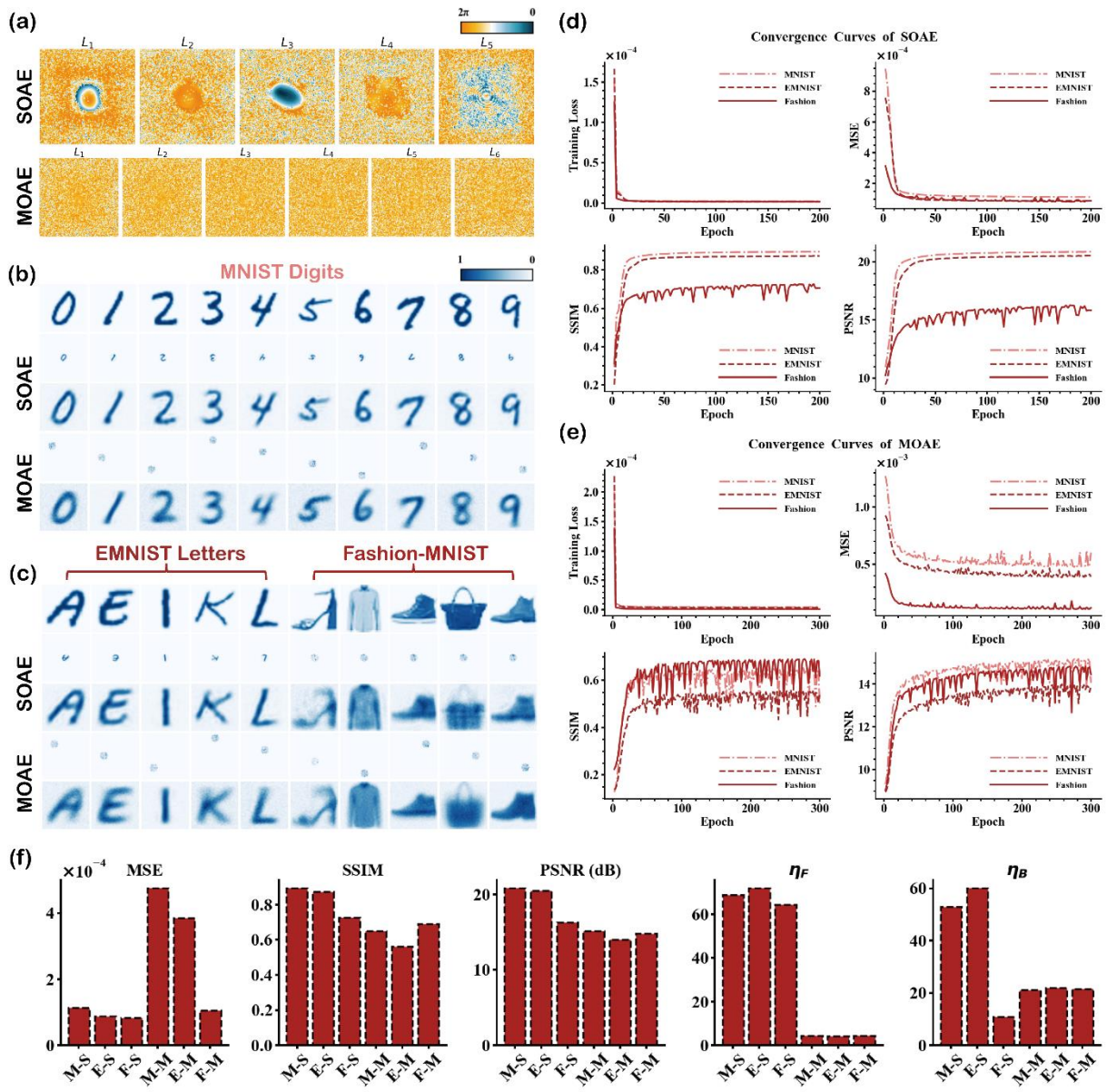


**Fig. 2 The results of the two basic modes, SOAE model and MOAE model.** (a) Phase profiles of for SOAE model and MOAE model trained on MNIST dataset. SOAE model is composed of five layers of phase-only modulation diffractive layers, while MOAE model consists of six layers. (b) The encoding (2nd row and 4th row) and decoding (3rd row and 5th row) results of two models for ten classes of samples from the MNIST dataset. The first row shows the ground truth. (c) The encoding and decoding results for five classes of samples from the EMNIST and Fashion datasets using two models. The models were trained on the ten-class datasets and the remaining five classes and model phase distributions are detailed in **Supplementary Fig. S1**. (d), (e) The training convergence curves of training losses and three evaluation metrics of the SOAE model and MOAE model, respectively. (f) The evaluation metrics for two models (abbreviation S and E) training on the MNIST (M), EMNIST (E), and Fashion (F) datasets.  $\eta_F$  and  $\eta_B$  are respectively forward and backward energy transmission efficiency (Details in **Methods and Materials**).

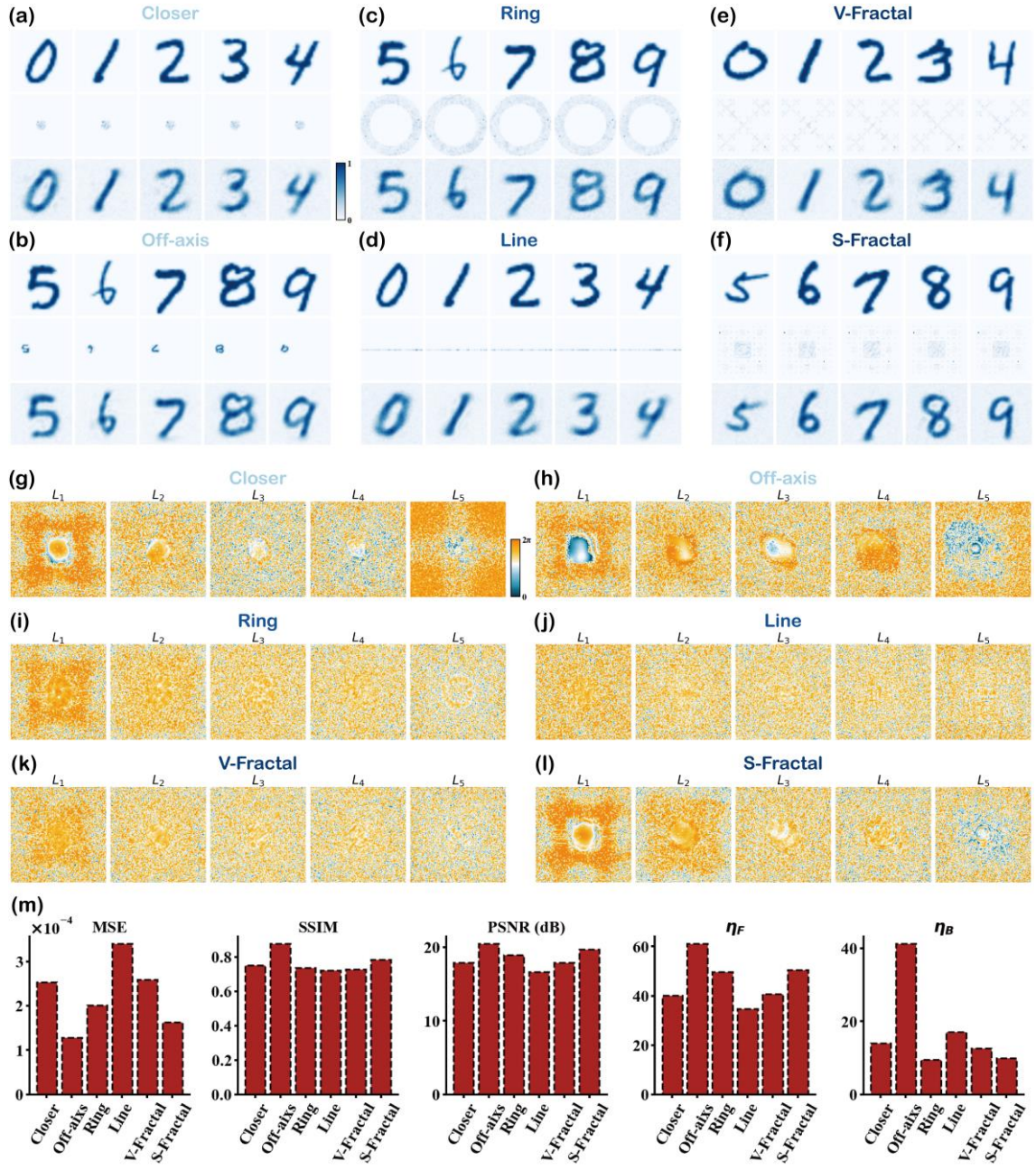


**Fig. 3 (a)-(f)** The encoding (2nd row) and decoding (3rd row) performance of six extended models on five categories of samples in the MNIST dataset. The results for the remaining five categories can be found in **Supplementary Fig. S4**. The first row shows the ground truth. **(g)-(l)** Phase distributions of six extended models. Each of these models consists of five layers of phase-only modulation diffractive layers. **(m)** Bar chart of evaluation metrics for the six extended models.

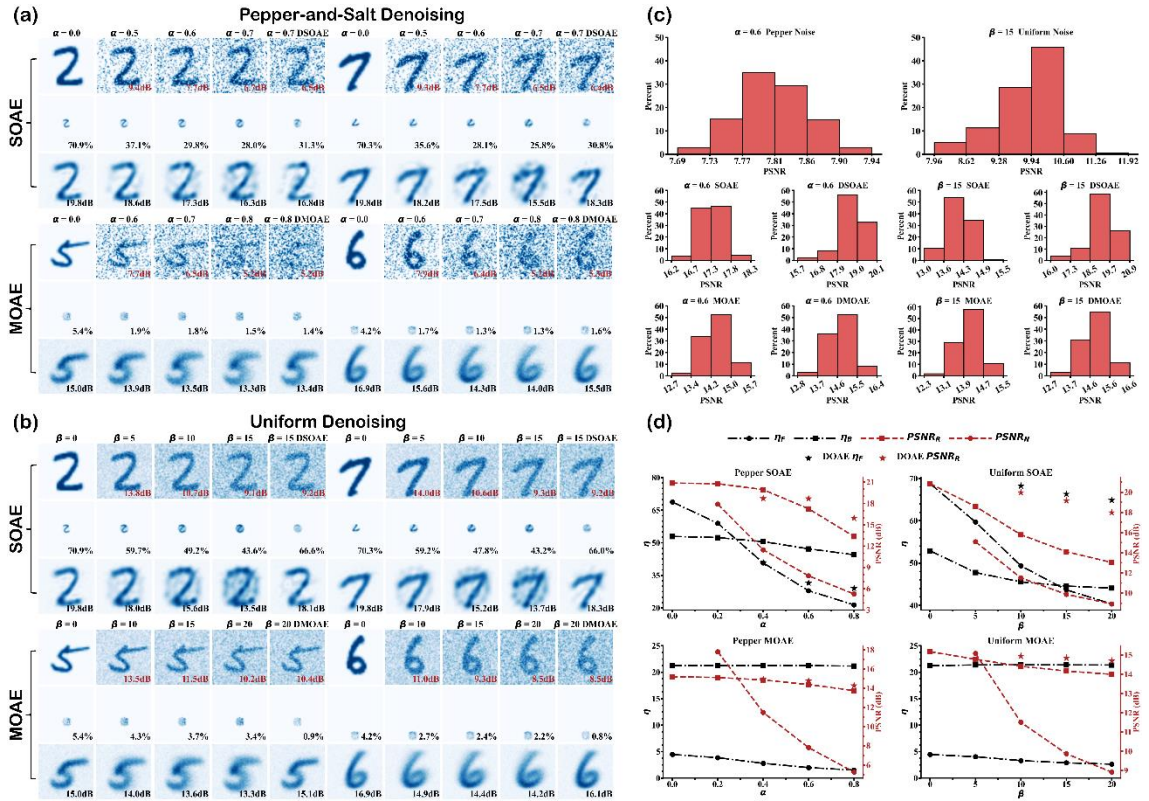


**Fig. 4 (a)** Results of the SOAE and MOAE models used to remove salt-and-pepper noise from images. The numbers in the lower right corners of the original and reconstructed images (1st, 3rd, 5th, and 7th rows) represent PSNR. The numbers in the same place of the encoded patterns (2nd and 5th rows) indicate forward transmission efficiency (similarly for **(b)**). Parameter  $\alpha$  determines the intensity of the injected salt-and-pepper noise (See **Materials and Methods Section**). DSOAE and DMOAE models are trained by images containing  $\alpha = 0.6$  noise. **(b)** Results of the SOAE and MOAE models used to remove uniformly distributed noise from images. Parameter  $\beta$  determines the intensity of the injected uniformly distributed noise (See **Materials and Methods Section**). DSOAE and DMOAE models are trained by images containing  $\beta = 10$  noise. **(c)** PSNR distribution histogram of images from the MNIST validation set corrupted by noise with  $\alpha = 0.6$  and  $\beta = 15$ , processed using the SOAE, MOAE, DSOAE, and DMOAE models. **(d)** Curves showing the variation of transmission efficiency and PSNR with noise intensity when using the SOAE and MOAE models to denoise salt-and-pepper noise and uniformly distributed noise.  $PSNR_R$  and  $PSNR_N$  are respectively PSNR of reconstructed images and noised images.

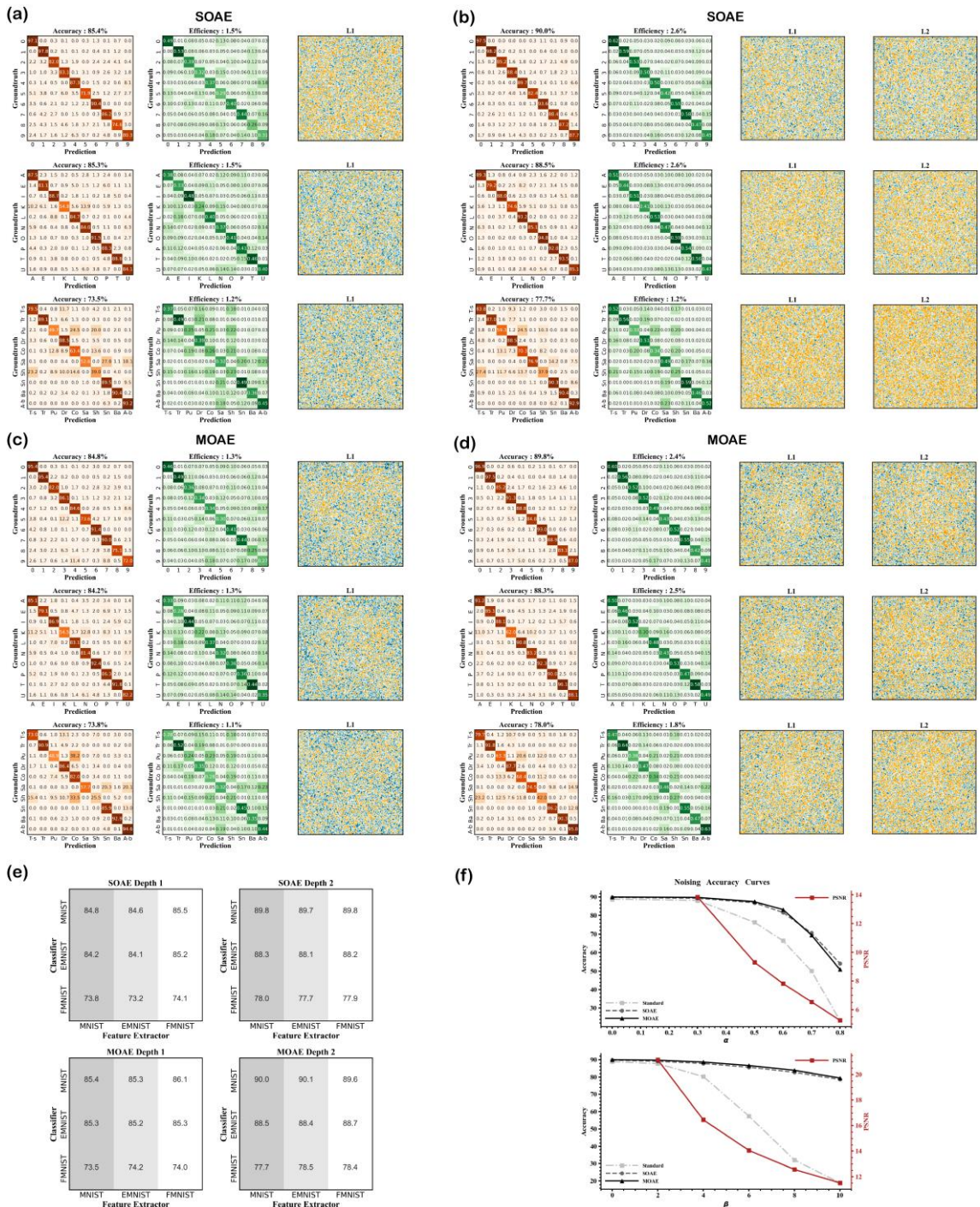


**Fig. 5 (a)-(d)** The accuracy confusion matrices, energy confusion matrices, and phase profiles of NRICs. The first, second, and third rows of each image respectively show the performance of MNIST-MNIST, MNIST-EMNIST, and MNIST-Fashion NRICs. **(a), (b), (c), and (d)** illustrate the classification results using SOAE encoder cascaded with a single classification layer, SOAE encoder cascaded with two classification layers, MOAE encoder cascaded with a single classification layer, and MOAE encoder cascaded with two classification layers, respectively. The focus pattern distribution for the ten categories is shown in **Supplementary Fig. Sx**. **(e)** The accuracy confusion matrices of all 36 types of NRICs (i.e., the combination of Classifier: MNIST and Feature Extractor: EMNIST in SOAE Depth 1 represents the SEMNIST-1MNIST NRIC). Detailed confusion matrices for the other 24 NRICs are shown in **Supplementary Figs. S7 and S8**. **(f)** The impact of noise intensity on classifier accuracy is demonstrated, where Standard refers to the normal classifier consisted of seven diffractive layers trained on MNIST dataset, SOAE and MOAE represent SMNIST-2MNIST and MMNIST-2MNIST NRICs, respectively.

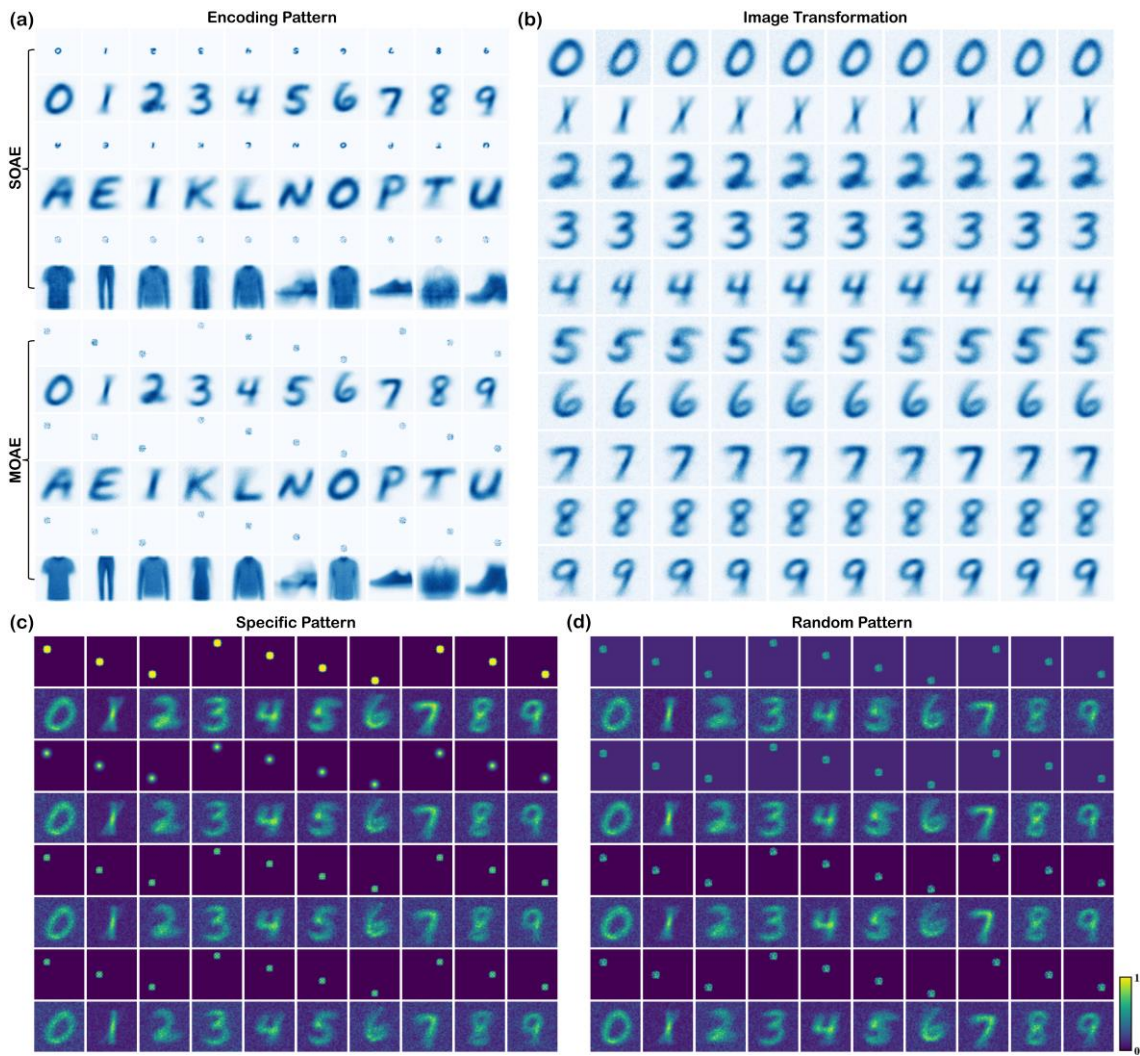


**Fig. 6** (a) Hologram generations using SOAE and MOAE models. 1st, 3rd and 5th rows display average encoded patterns of MNIST, EMNIST and Fashion datasets, respectively. 2th, 4th and 6th rows show the corresponding generated holograms. (b) Image transformations of MNIST dataset based on well-trained MOAE generator (i.e., The transformation of number 0 to number 1 was achieved as follows. Firstly, get ten average encoded patterns of number 0 class. Then, only take the pattern at second place corresponding to number 1 class as input of generator to produce hologram of number 1.). The first column shows the transformations from number 0 to other numbers and the same goes for the other columns. Image transformations of EMNIST and Fashion datasets are shown in **Supplementary Fig. S9**. (c)-(d) Conditional hologram generation of MNIST dataset using well-trained MOAE generator. The input patterns of generator are shown in 1st, 3rd, 5th and 7th rows. The patterns in the same row are identical in content, differing only in their positions. The specific patterns of (c) respectively conform to constant, Gaussian, cosine and sine functions and the random patterns of (d) are sampled from normal distributions (1st and 3rd rows) and uniform distributions (5th and 7th rows). 2th, 4th, 6th and 8th rows present the generated holograms. Conditional hologram generations of EMNIST and Fashion datasets are shown in **Supplementary Fig. S10**.

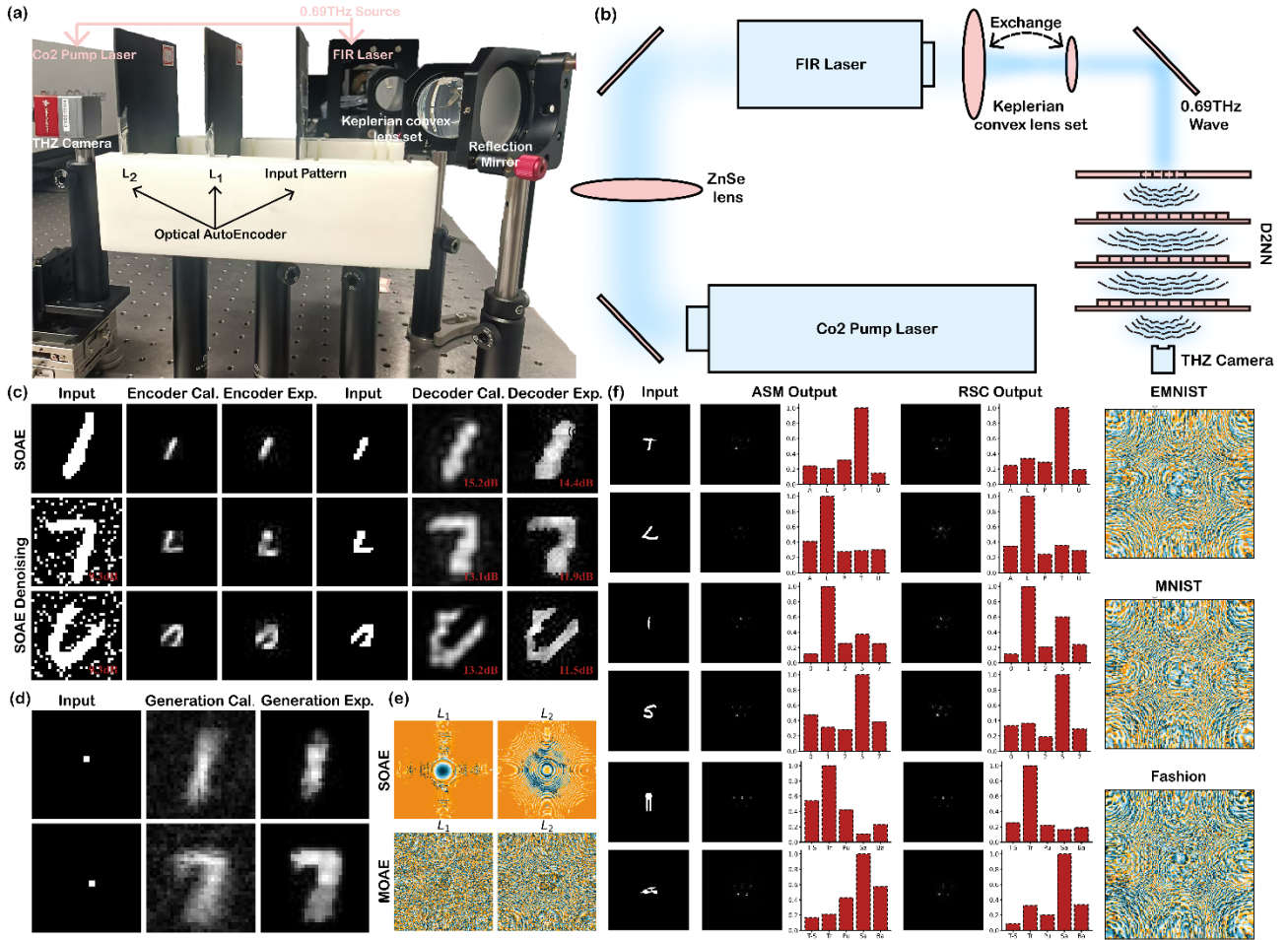


**Fig. 7** **(a)** Actual optical path diagram of the THz verification experiment. **(b)** Conceptual schematic diagram of the THz verification experiment. After the THz laser was emitted from the FIR laser, it passed through a lens group to adjust the aperture size. Then, it entered the D<sup>2</sup>NN after reflection. Finally, it was modulated by the D<sup>2</sup>NN and imaged at the camera plane. **(c)** Experimental verification results of the SOAE model. For the convenience of the experiment, the encoded patterns were obtained by binarizing the numerical patterns. **(d)** Experimental verification results of the CHGs using MOAE model. **(e)** Height profiles of the MOAE and SOAE models. **(f)** Verification results of the NRICs using precise numerical calculation method and their classification layer height profiles.